Shallow Damage Zone Structure of the Wasatch Fault in Salt Lake City from Ambient-Noise Double Beamforming with a Temporary Linear Array

Konstantinos Gkogkas*[1], Fan-Chi Lin[1], Amir A. Allam[1], and Yadong Wang[2]

Abstract

We image the shallow structure across the East Bench segment of the Wasatch fault system in Salt Lake City using ambient noise recorded by a month-long temporary linear seismic array of 32 stations. We first extract Rayleigh-wave signals between 0.4 and 1.1 s period using noise cross correlation. We then apply double beamforming to enhance coherent cross-correlation signals and at the same time measure frequency-dependent phase velocities across the array. For each location, based on available dispersion measurements, we perform an uncertainty-weighted least-squares inversion to obtain a 1D V_S model from the surface to 400 m depth. We put all piece-wise continuous 1D models together to construct the final 2D V_S model. The model reveals high velocities to the east of the Pleistocene Lake Bonneville shoreline reflecting thinner sediments and low velocities particularly in the top 200 m to the west corresponding to the Salt Lake basin sediments. In addition, there is an $\sim$400–m–wide low-velocity zone that narrows with depth adjacent to the surface trace of the East Bench fault, which we interpret as a fault-related damage zone. The damage zone is asymmetric, wider on the hanging wall (western) side and with greater velocity reduction. These results provide important constraints on normal-fault earthquake mechanics, Wasatch fault earthquake behavior, and urban seismic hazard in Salt Lake City.

Cite this article as Gkogkas, K., F.-C. Lin, A. A. Allam, and Y. Wang (2021). Shallow Damage Zone Structure of the Wasatch Fault in Salt Lake City from Ambient-Noise Double Beamforming with a Temporary Linear Array, *Seismol. Res. Lett.* **XX**, 1–11, doi: 10.1785/0220200404.

Introduction

Seismic tomography using surface waves from ambient-noise cross correlations has emerged as a useful tool over the past decades for imaging the Earth's interior structure (e.g., Shapiro *et al.*, 2005; Lin *et al.*, 2009; Shen *et al.*, 2013; Nakata *et al.*, 2015; Li *et al.*, 2016; Spica *et al.*, 2016; Berg *et al.*, 2020). By exploiting natural vibrations to extract empirical Green's functions (e.g., Lobkis and Weaver, 2001), ambient-noise tomography has the advantages of not relying on the availability of ballistic active or passive sources. Combined with the recent development of portable low-cost temporary seismic instrumentation, it is now possible to acquire unprecedented high-resolution data in previously difficult or inaccessible regions providing new insight for seismic hazard assessment (Lin *et al.*, 2013; Bowden *et al.*, 2015; Nakata *et al.*, 2015; Clayton, 2020; Castellanos *et al.*, 2020), tectonic processes (Wang *et al.*, 2019b), earthquake mechanics (Roux *et al.*, 2016; Mordret *et al.*, 2019; Li *et al.*, 2019; Wang *et al.*, 2019b), volcanic structures (Brenguier *et al.*, 2016; Nakata *et al.*, 2016; Wang *et al.*, 2017; Ranasinghe *et al.*, 2018; Wu *et al.*, 2020), reservoir monitoring (De Ridder and Biondi, 2013), landslides (Thomas *et al.*, 2020), critical zones (Keifer *et al.*, 2019), and hydrothermal dynamics (Wu *et al.*, 2017; Wu *et al.*, 2019). In particular, it is well established that the shallow shear-velocity structure greatly affects the amplitudes of seismic waves (Tinsley *et al.*, 1991), making shallow seismic imaging a critical component of seismic hazard assessment (e.g., Graves *et al.*, 2011; Fu *et al.*, 2017).

The Salt Lake City (SLC) (Utah, U.S.A.) metropolitan area is situated in the Salt Lake basin, a Cenozoic lacustrine and fluvial basin bounded by the normal-fault horsts of the Wasatch (east) and Oquirrh (west) mountains (Stokes, 1980). The upper few hundred meters of the basin comprise late Pleistocene, Lake Bonneville, unconsolidated sediments (Kowalewska and Cohen, 1998), which can dramatically amplify coseismic shaking (e.g., Johnson and Silva, 1981; Moschetti *et al.*, 2017). With a population of ~1.2 million and an ~70% chance of a

1. Department of Geology and Geophysics, University of Utah, Salt Lake City, Utah, U.S.A.; 2. Halliburton R&D, Singapore, Singapore

*Corresponding author: gkogkaskonstantinos@gmail.com

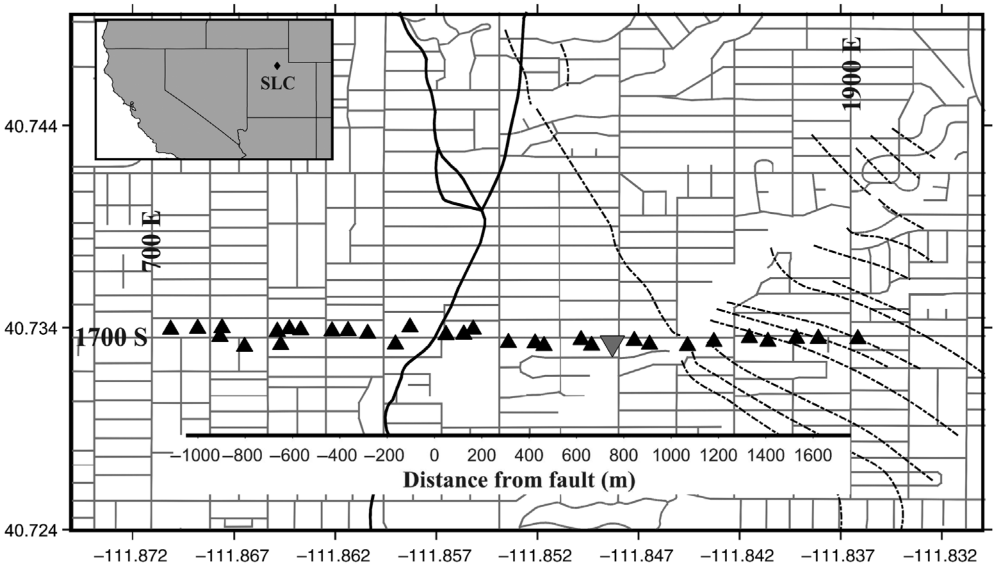

Figure 1. Street map of Salt Lake City (SLC) along 1700 South Street, showing station locations (black triangles) of the temporary network. The surface trace of the East Bench fault (EBF) of the Wasatch fault system is shown with black solid lines (McKean, 2018; McDonald *et al.*, 2020). The retrogressive phases of the Provo shoreline are shown with dotted lines (McKean, 2018). The upside-down triangle shows the virtual source station location used in the record sections of Figure 2. Few major streets mentioned in the Data and Methods section are identified. Inset plot: Map of western US where the location of Salt Lake City is indicated by a diamond.

damaging earthquake in the next 50 yr (Petersen *et al.*, 2020), the region represents some of the highest risk potential in the conterminous United States. The overall basin structure has long been constrained by geologic mapping (Gilbert, 1890) and borehole data (Kowalewska and Cohen, 1998), including three major paleoshorelines of Lake Bonneville (Oviatt, 2015). The mechanical properties are less defined (Magistrale *et al.*, 2009), because the sediments are prone to highly variable amplification during earthquake shaking (Tinsley *et al.*, 1991).

The fault system that contributes most to the seismic potential in the area is the north–south-striking Wasatch fault system (WFS). The WFS comprises 10 segments with total length of more than 350 km, and is the largest normal fault in North America as part of the intermountain seismic belt, which bounds the eastern edge of the Basin and Range Province. Recent acquisition and analysis of light detection and ranging data (McDonald *et al.*, 2020) provide newly mapped fault scarps across the WFS segments and extends the surface traces of known faults. Paleoseismic studies of the WFS (DuRoss *et al.*, 2016) have identified six events with $M > 6$ in the last 5000 yr. The East Bench fault (EBF; surface mapping by McKean 2018; McDonald *et al.*, 2020) is a subsystem of the Salt Lake segment of the WFS expressed as a series of en echelon west-dipping faults that cross the SLC metropolitan area. Active-source seismic surveys in the area (Liberty *et al.*, 2018a) have identified the shallow expression of fault traces and relates velocity structure to the hydrostratigraphy of the area.

In this study, we use data from a temporary linear nodal array that was deployed across 1700 South Street in SLC. The array cut across both the EBF and the Provo shoreline (Fig. 1), one of the major paleoshorelines of Lake Bonneville (Oviatt, 2015). First, we compute the cross-correlation functions and use vertical–vertical cross correlations to extract Rayleigh waves propagating along the line. A challenge in our analysis is the presence of non-diffusive noise in the ambient wavefield, likely relative to urban activities. To enhance the signal and measure phase velocities across the linear array, we use the double-beamforming method developed by Wang *et al.* (2019a,b), which has been successfully applied to both regional (Cascadia; Wang *et al.*, 2019a) and local scales (San Jacinto fault; Wang *et al.*, 2019b). In this study, we apply the method to study the shallow structure and simultaneously test its performance in an inland urban environment. After we measure period-dependent phase velocities, we invert the dispersion curve at each location for a 1D V_S model using the weighted least-squares approach described by Herrmann (2013). Finally, we combine all 1D V_S models to produce a 2D V_S model across the array.

Data and Methods

A network of 32 nodal stations was deployed along 1700 South Street in SLC from 8 February to 12 March 2018 (station locations shown in Fig. 1; Lin, 2018). The linear array had an ~2.9 km aperture and spanned from 700 East to 1900 East Street. The availability of deployment locations—primarily local volunteer homeowners—resulted in some irregularity in station spacing with variation from ~10 to ~100 m.

Noise cross correlations

We compute ambient-noise cross correlations following Wang *et al.* (2019a). Examples of the vertical–vertical ($Z-Z$) cross-correlation record sections between a common station (virtual source) close to the array center and all other receiver stations across the array are shown in Figure 2, band-passed near 0.9 s (Fig. 2a) and 0.4 s (Fig. 2b). The observed Rayleigh-wave signal moveout is asymmetric, indicating stronger seismic energy propagating to the east. Besides the primary Rayleigh-wave

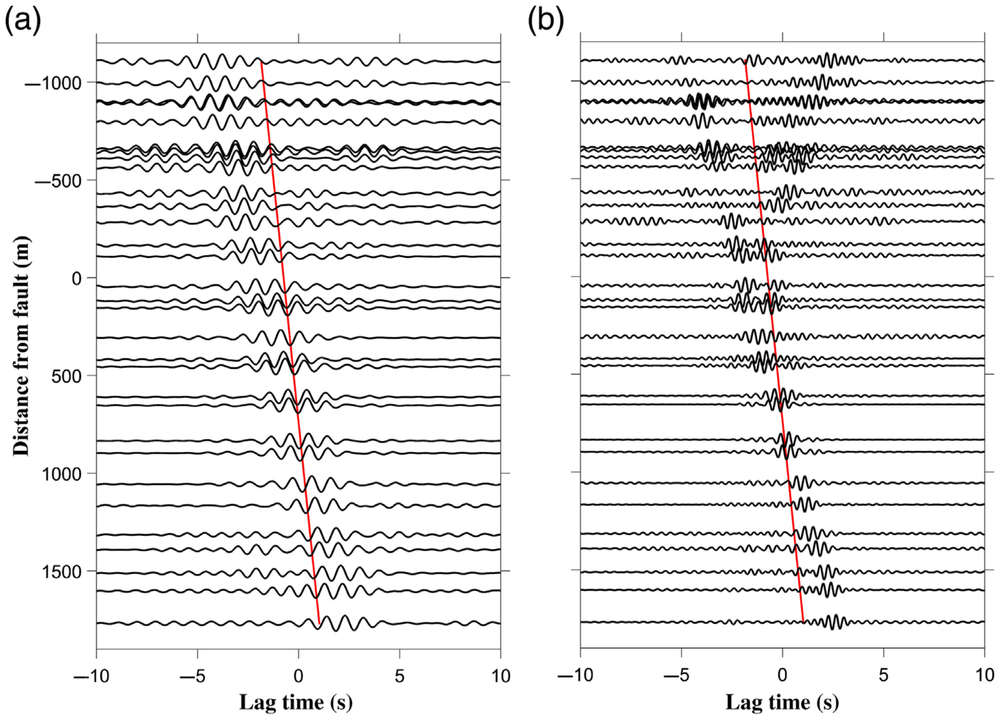

Figure 2. Vertical–vertical cross-correlation functions between a virtual source station (gray reversed triangle in Fig. 1) and all the array receivers, band-passed (a) near 0.9 s and (b) near 0.4 s. Solid line depicts a reference velocity line (1 km/s). Rayleigh-wave signal moveout is observed in the record sections with the dominant energy propagating toward the east. The color version of this figure is available only in the electronic edition.

signals, secondary signals are also observed especially at shorter periods (Fig. 2b), likely due to the presence of persistent noise sources or active scatterers (Ma *et al.*, 2013) in the vicinity of the study area. Although determining the nature of these secondary signals is out of the scope of our current study, future 2D dense array deployment in the area would allow us to study the radiation pattern in detail and determine if the phase is fault-zone related.

Double-beamforming tomography

To enhance the coherent Rayleigh-wave signals and measure phase velocities, we follow Wang *et al.* (2019a,b) and perform double beamforming. We form source and receiver beams across the array with a fixed 250 m beam width and 50 m beam center spacing. The beam width was chosen here to be large enough to include a sufficient number of stations (at least three stations in both the source and receiver beams). The beam width also intrinsically controls the lateral smoothing applied by the method. We adopt a less strict far-field criterion to remove all beam pairs with distance between the source and the receiver beam center smaller than either 1 or 1.5 wavelengths for periods between 1.1–0.7 and 0.6–0.4 s, respectively. Here, we use a 1 km/s reference velocity to estimate the wavelength. The slightly looser criterion for longer periods is because of the limited array aperture and hence the number of beam pairs passing the selection criterion. The application of this distance criterion can still result in including individual station pairs with distance smaller than 1 or 1.5 wavelengths, but we see no obvious disturbance to the observed Rayleigh-wave moveout when including those short-distance pairs. Following Wang *et al.* (2019a), we assume planar wavefront geometry and no off-great-circle propagation.

For each source–receiver beam pair, we first cut and taper the cross-correlation waveforms based on an empirically determined period-dependent maximum group velocity (0.5–1.1 km/s). Following Wang *et al.* (2019b), we then shift and stack the waveforms in the frequency domain (Fig. 3a) using different source (u_s) and receiver (u_r) phase slowness combinations, ranging from 0.4 to 5 s/km. We measure the phase slowness on both source and receiver sides using a two-step grid search (coarse and finer grid, Wang *et al.*, 2019b) based on the maximum amplitude of the stacked waveform (beampower; example shown in Fig. 3b). To ensure that the grid search is picking the energy packet corresponding to the fundamental mode Rayleigh-wave signal, we require the dispersion measurements to be continuous across different periods. We first determine the phase slowness at periods longer than 0.9 s in which signals are clean and simple. Starting at 0.9 s, we then use the slowness from the period immediately above as the reference slowness. Only source and receiver slowness measurements within 25% of their corresponding reference slowness are accepted.

After performing the grid search for all source and receiver beam pairs across the array, the phase slowness at each location (i.e., each beam center) is determined by the mean of measurements at that location with different source-receiver beam combinations. Measurements outside of two standard deviations (st.dev.) are considered as outliers and removed. The uncertainty for each location is computed as the st.dev. of the mean divided by the square root of independent measurements (Fig. 4a), defined as the number of nonoverlapping beams (Wang *et al.*, 2019a). To account for potential systematic biases due to an uneven source distribution, we set the minimum uncertainty

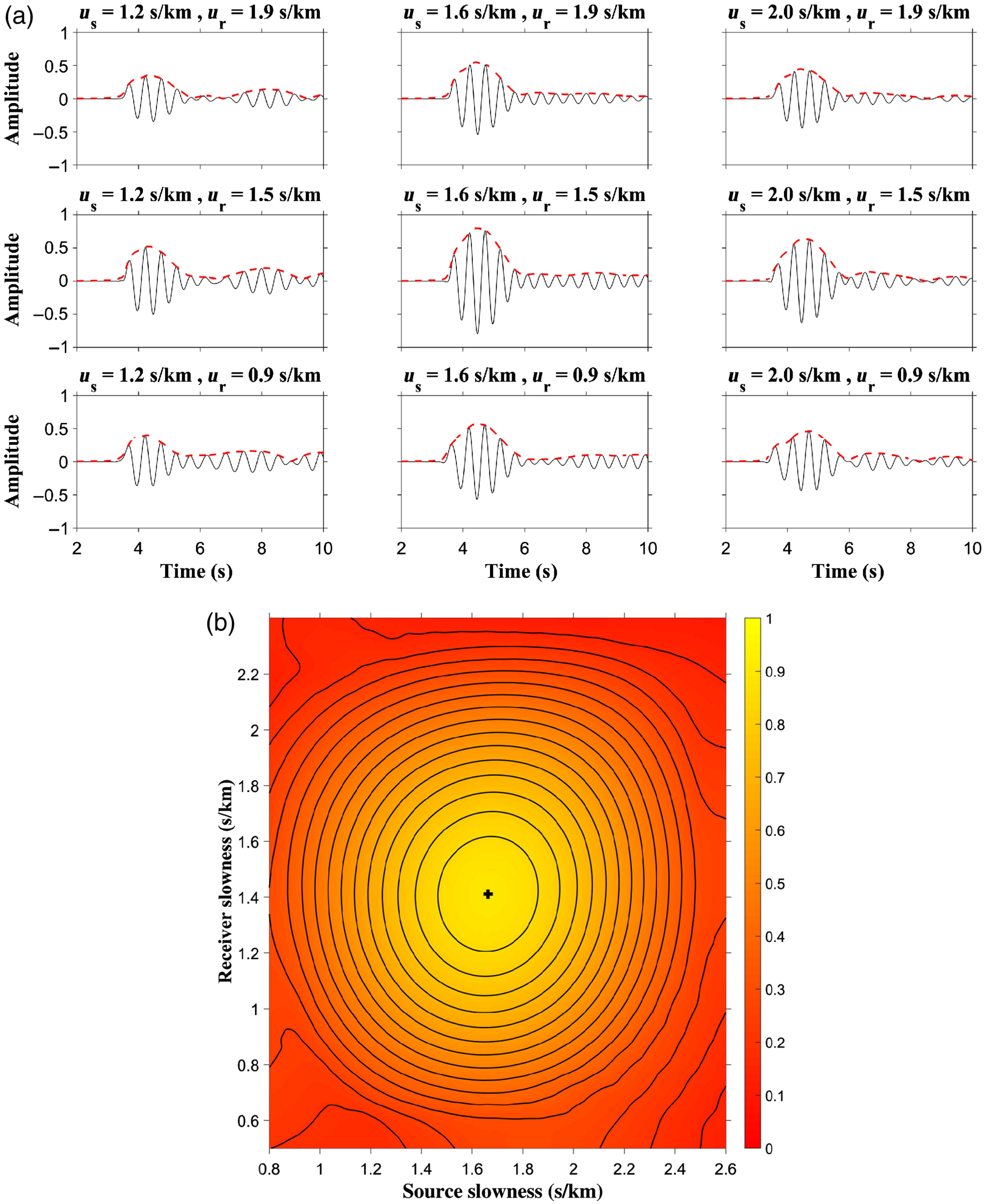

Figure 3. Example of the waveform shift and stacking procedure and the 2D grid search for a beam pair at 0.5 s, in which the source beam center is located at −0.6 km and the receiver beam center is located at 1.25 km along the linear array (Fig. 2). (a) Stacked waveforms after shifting using different source (u_s) and receiver (u_r) phase slowness combinations. Dashed lines indicate the envelope function of each stacked waveform. (b) Beampower plot with varying source and receiver slowness. The black cross denotes the location of maximum beam amplitude. Iso-amplitude contours are plotted as black lines using 0.05 interval. The color version of this figure is available only in the electronic edition.

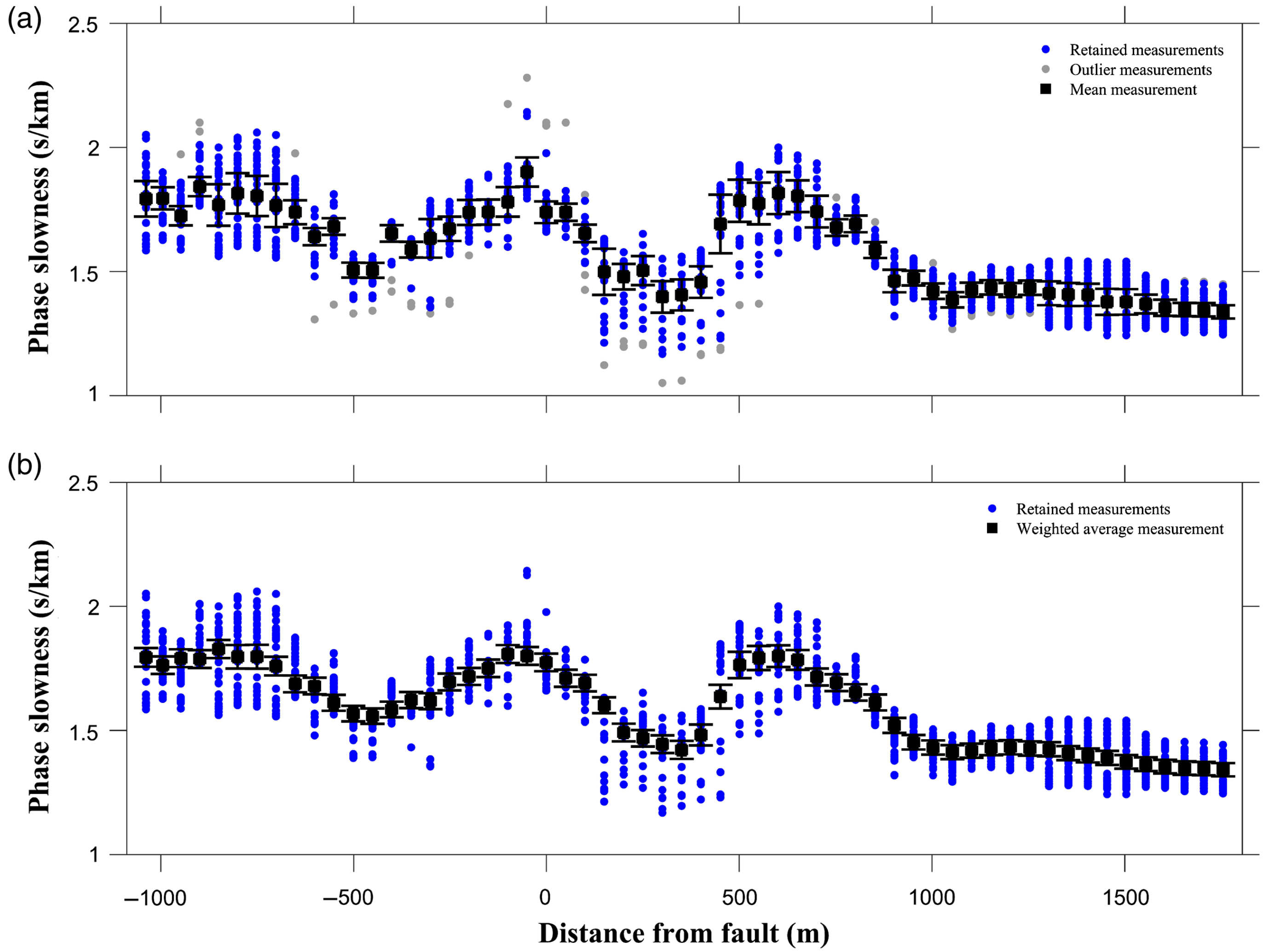

Figure 4. Phase slowness profiles for 0.5 s period. Phase slowness measurements not satisfying the SNR criterion are not shown. (a) Profile before smoothing and (b) profile after smoothing. The color version of this figure is available only in the electronic edition.

as 2% of the mean. In addition, we perform signal-to-noise ratio (SNR; Lin *et al.*, 2009) calculations based on the stacked waveform and remove spurious measurements with SNR smaller than 5. We define SNR as the peak-stacked waveform amplitude within the signal window (velocity between 0.3 km/s and an empirically determined period-dependent maximum velocity between 0.5 and 1.1 km/s) divided by the root mean square of the noise window (20 s following the signal window). Considering the irregular station spacing and the significant beam overlap, we further smooth the phase slowness profile for each period. The smoothed phase slowness and uncertainty at each location is computed as the weighted average of the three neighboring points (the three locations are 50 m apart) and the standard error of the weighted average, respectively (Fig. 4b). The phase slowness and their uncertainties for all periods are combined and converted into phase velocity (Fig. 5a) and uncertainty (Fig. 5b) profiles before shear-velocity inversions are performed. The overall slower phase velocities to the west and faster phase velocities to the east likely reflect the thickening of sediments toward the center of the basin. On a smaller scale, a localized slow anomaly is observed near the surface trace of the EBF. The anomaly is wider at shorter periods and narrower at longer periods (0.8–1.1 s) potentially related to the depth-dependent fault-zone damage structure.

Shear-velocity inversion

To invert for a 2D V_S model across the nodal array, we first extract the Rayleigh-wave phase velocity dispersion curve at each location across the profile. Then, we invert each dispersion curve independently using the iterative weighted least-squares algorithm of Herrmann (2013) to obtain a 1D V_S model. Following Wang *et al.* (2019b), we use a homogeneous starting model with fixed V_P/V_S ratio equal to 1.75 and an empirical density calculated from V_P using the relationship of Brocher (2005). Based on the geological setting

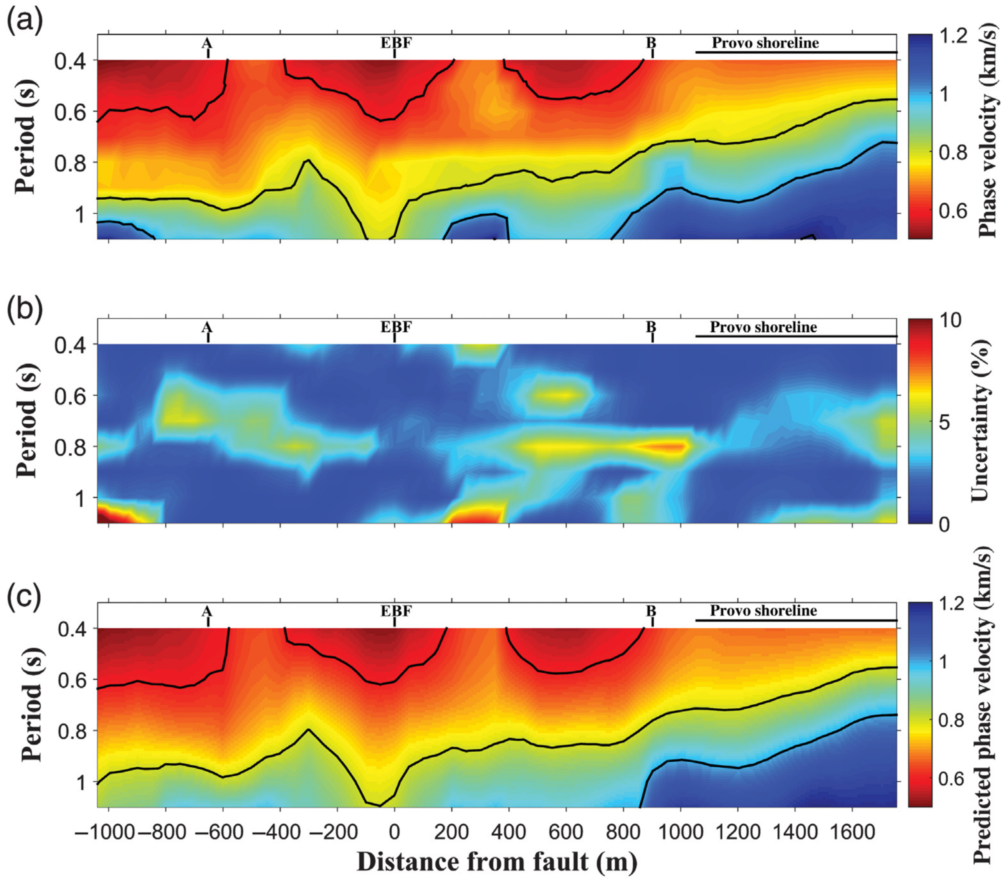

Figure 5. (a) Phase-velocity map, (b) uncertainty map, and (c) predicted phase-velocity map calculated from the inverted 2D V_S model. Phase-velocity contours are separated by 200 m/s. The two example locations (A and B) used in Figures 6 and 7 are also denoted.

in the area, we impose a monotonically increase constraint to the inverted 1D shear velocity models. We allow the inversion to iterate up to 80 times to get the final 1D V_S model, but stop the iteration when the chi-square misfit does not improve by more than 1% compared to the previous iteration. On average, the inversion stopped after ~18 iterations.

Examples of local dispersion curves and their inverted V_S models are shown in Figure 6. The shear-velocity model for location A (Fig. 6a, −0.55 km distance) is generally slower compared to location B (Fig. 6c, 0.9 km distance). This is somewhat expected as location B is closer to the eastern basin edges and hence has thinner soft sediment. The observed phase velocity dispersion curves in general can be fitted well by the model predicted dispersion curves in which discrepancies are mostly smaller than the estimated measurement uncertainties. We only consider the top 400 m of the inverted models robust considering the overall depth sensitivity of our measurements (Fig. 7). We combine all 1D V_S models across the profile to create a 2D V_S model (Fig. 8). The predicted phase-velocity profile (Fig. 5c) closely resembles the observed profile (Fig. 5a) with only noticeable differences where uncertainties are high.

Results and Discussion

The 2D shear-velocity model (Fig. 8) exhibits similar spatial patterns to the phase-velocity map (Fig. 5a). The overall trend in the V_S profile is decreasing velocity to the west likely corresponding to sedimentary thickening toward the center of the basin (Radkins et al., 1989; Hill et al., 1990). The decreasing velocity may also represent changes in the overall composition of the shallow lacustrine deposits, which transition from younger and softer clay, silt, and fine sand in the west to older and mechanically stronger sand and gravel toward the east (McDonald and Ashland, 2008). The highest velocities (>1.2 km/s) in the model observed at depth in the east end of our model potentially mark the transition between shallow unconsolidated Quaternary sediments and deeper Tertiary strata, comprised of volcanic and plutonic rocks (Liberty et al., 2018b). The basin bedrock formations with shear velocities greater than 3 km/s suggested by previous geophysical studies in the area (Bashore, 1982; Hill et al., 1990; Mabey, 1992; Magistrale et al., 2009) are likely below our maximum resolved depth; a future study with a larger array aperture is needed to constrain the deeper basin structure.

The EBF is expressed in the period-dependent phase velocity (Fig. 6) and final V_S profiles (Fig. 8) as a narrow asymmetric low-velocity zone. Large-scale seismogenic faults are well known to produce low velocities in their vicinity by breaking surrounding rock during coseismic shaking (e.g., Ben-Zion and Sammis, 2003); these features are termed "damage zones" and are typically on the order of tens to hundreds of meters wide depending on the size of the largest earthquakes (Faulkner et al., 2011), depth of the seismogenic zone (Ampuero and Mao, 2017), cumulative fault slip (Sagy et al., 2007; Perrin et al., 2016), and local rheology (e.g., Finzi et al., 2009; Molli et al., 2010; Thakur et al., 2020). In addition to the main mapped trace of the EBF, there are two other similar low-velocity zones (−1000 to −600 m and 400 to 800 m relative to EBF), which likely correspond to other strands within the Wasatch fault zone; large-scale normal

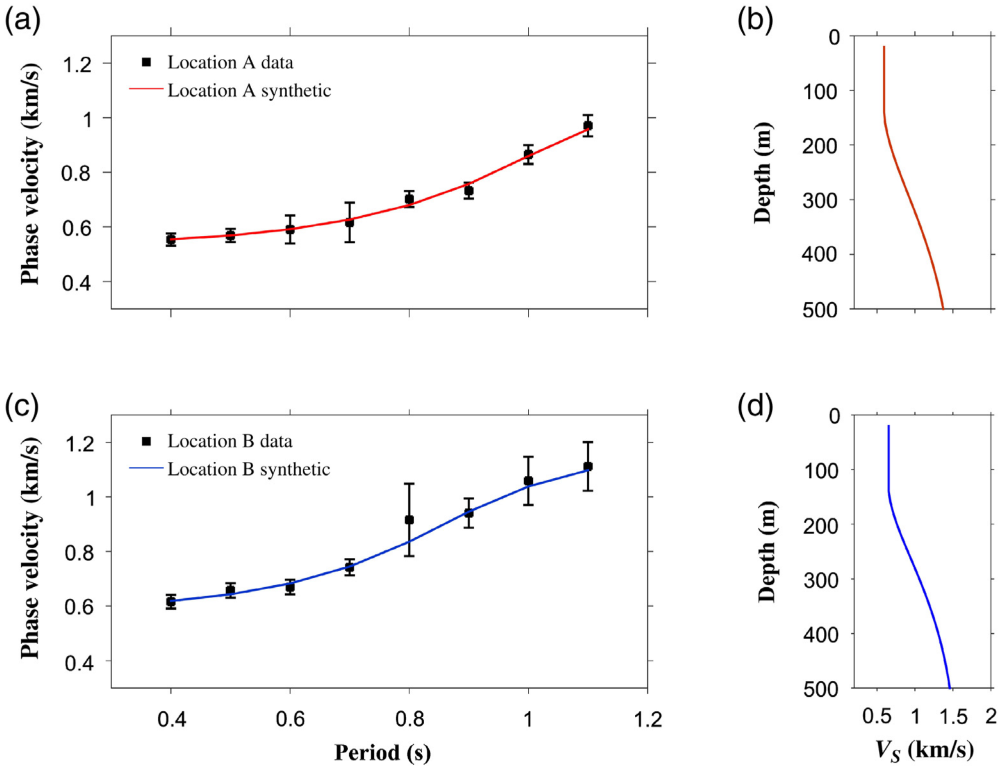

Figure 6. (a) Comparison between measured and synthetic dispersion curves at −0.65 km from EBF. (b) The inverted 1D V_S model at −0.65 km. Panels (c,d) are same as panels (a,b) but at 0.9 km from EBF. Error bars demonstrate uncertainties times 2. The color version of this figure is available only in the electronic edition.

faults are expected to branch into "flower structures" at shallow depths due to the reduced normal stress (e.g., Twiss *et al.*, 1992; chapter 5). Previous active-source imaging in the same area resolved 11 fault strands across a 4.5 km linear array, only one of which was mapped at the surface (Liberty *et al.*, 2018b). We acknowledge that the observed localized low-velocity zones can also be related to other factors (Wang, 2001), including differences in sediment compaction rate and lithology (e.g., Olig *et al.*, 1996), layering-induced anisotropy (e.g., Behera *et al.*, 2011), and increased porosity, pore-fluid saturation (e.g., Shimeld *et al.*, 2016). In addition, the low-velocity anomalies may represent remnant liquefaction areas from past earthquakes (e.g., Liberty *et al.*, 2018a), and also be affected by interbedded smaller-scale structures such as colluvial wedges (e.g., Buddensiek *et al.*, 2008) with increasing thickness proportional to past earthquake magnitude (e.g., Morey and Schuster, 1999). Additional ground truth information (e.g., drilling cores) will be required to distinguish these interpretations.

The increasing normal stress with depth also leads to a narrower damage zone with depth (e.g., Allam and Ben-Zion, 2012), either due to inhibited mode I fracture growth (e.g., Prudencio and Van Sint Jan, 2007) or due to enhanced rock healing with increasing temperature (Lyakhovsky and Ya Hamiel, 2007). The main trace of the EBF observed here (Fig. 8) narrows with depth from ∼600 m width at the surface to ∼300 m width at the bottom of the resolved profile. The inferred damage zone is asymmetric with respect to the surface trace of the fault, with more and higher intensity damage in the hanging wall. This pattern is expected for normal faults and has previously been observed both geologically (Flodin and Aydin, 2004; Berg and Skar, 2005) and in numerical simulations of dipping faults (Xu *et al.*, 2015). Because of the complicated damage pattern and the limited resolution of our tomographic image, it is difficult to constrain the precise dip of the EBF and other subsidiary strands from our result. However, the central portion of the damage zone is either vertical or dipping slightly to the west. If this is the case, it is further support for a listric structure to the Wasatch fault zone (Mohapatra and Johnson, 1998; Pang *et al.*, 2020), listric structure to normal faults more generally (Wernicke, 1981; Davison 1986; Bose and Mitra, 2010), and is in line with free-surface orthogonality expectations from Andersonian faulting theory (Leung and Su, 1996).

The Provo shoreline is observed as a sharply bounded high-velocity region in the east within our 2D V_S model (Fig. 8) with much higher velocity at all resolved depths (particularly at depth). Because of this relatively sharp lateral boundary, which persists to at least 400 m depth, we interpret this boundary as an additional fault strand related to the EBF or Wasatch fault zone more generally. Previously imaged non-fault shoreline boundaries in SLC have gradually thickened sediments westward from the shoreline (Liberty *et al.*, 2018b). A recent geodetic study (Hu *et al.*, 2018) indicates that the EBF is also hydrological boundary controlling surface deformation in the area.

Conclusions

We present new results of noise-based shallow imaging in Salt Lake Valley near the vicinity of the EBF using a dense linear array. We enhanced our noise cross-correlation signals and measured Rayleigh-wave phase velocities between 0.4 and 1.1 s period across the array using the double beamforming method

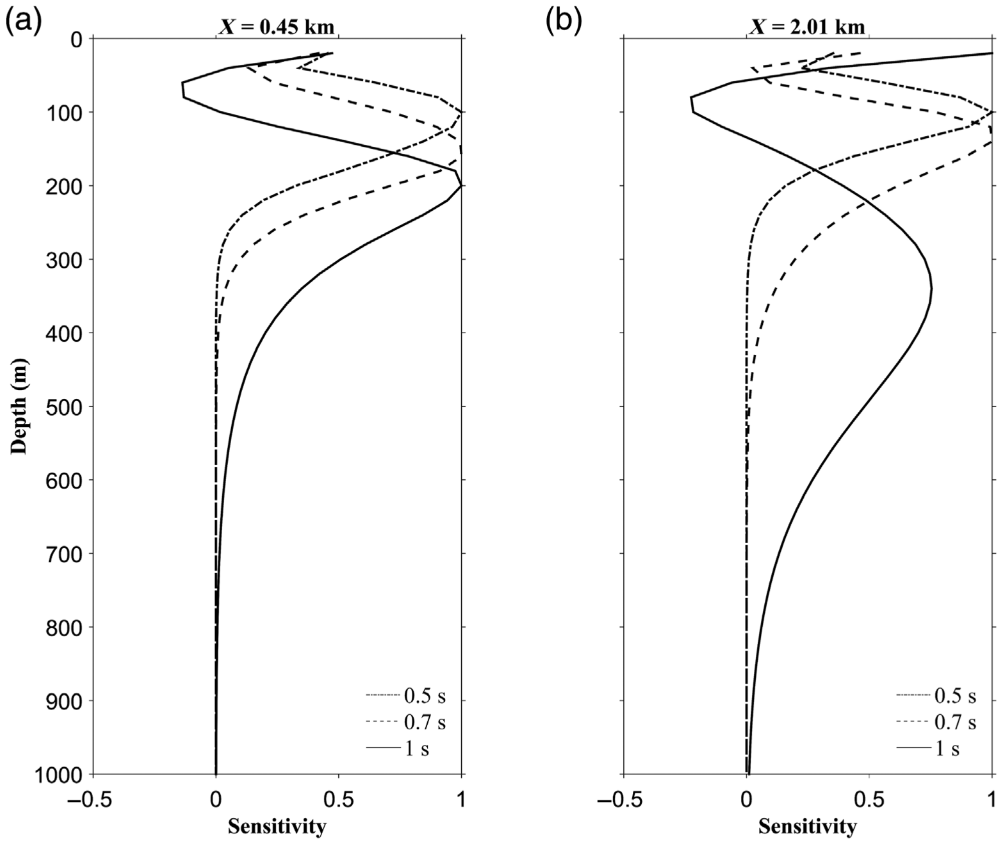

Figure 7. V_S sensitivity kernels for Rayleigh-wave phase velocity at 0.5, 0.7, and 1 s periods at two example locations. (a) –0.65 km and at (b) 0.9 km from EBF.

narrower with depth. The resolution achieved in this study enabled the imaging of this low-velocity fault-zone structure for the first time, because its spatial extent is smaller than the resolution limit of previous studies (e.g., Hill *et al.*, 1990; Magistrale *et al.*, 2009). Our results, along with other recent studies (Liberty *et al.*, 2018a; McDonald *et al.*, 2020; Pang *et al.*, 2020), indicate that the fine-scale structure of the WFS is a complicated series of fault strands and their associated damage. The success of this study motivates future work in the area to better understand the structure and the seismic hazard associated with the WFS. The deployment of a network with wider aperture and in 2D is needed to study the WFS at greater depth, constrain its lateral variation, and better understand the SLC urban noise characteristics.

(Wang *et al.*, 2019). Despite the less known and potentially complex noise wavefield associated with the inland metropolis, the observed phase velocity profile and 2D V_S model constructed between the surface and 400 m depth are consistent with the geologic and the geotectonic models of the area. This indicates the ability of the method to produce reliable shallow crustal images even in an urban environment far away from the ocean microseism. We provide new constrains on the shallow structure of the EBF, which has an ~400 m damage zone that gets

Data and Resources

Seismic data from this network (DOI: 10.7914/SN/9H_2018) will be available to download from Incorporated Research Institutions for Seismology (IRIS). Resources used for maps are available from the Utah Automated Geographic Reference Center (AGRC) (https://gis.utah.gov/) and the Utah Geological Survey (UGS). The surface wave inversion tool used in this study is part of "Computer Programs in Seismology" (Herrmann, 2013) and available from http://www.eas.slu.edu/eqc/eqccps.html. All websites were last accessed in October 2020.

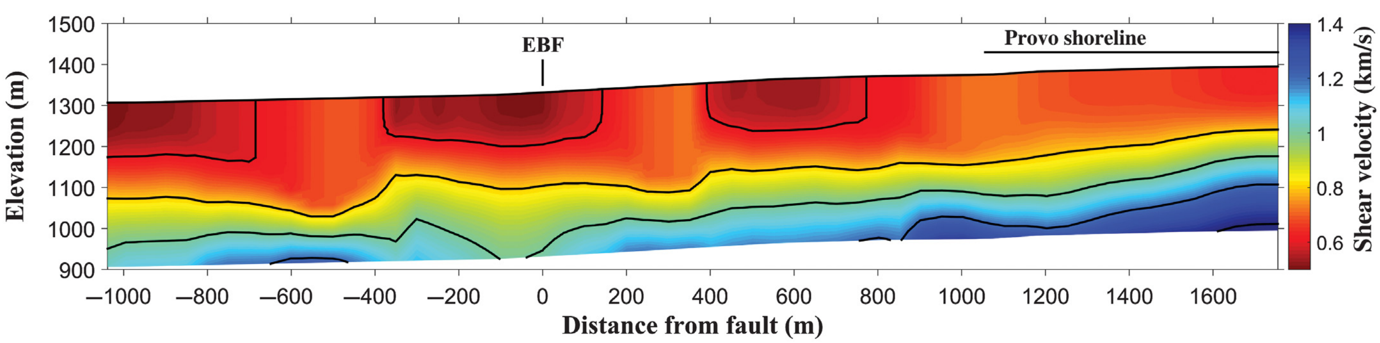

Figure 8. 2D shear-velocity model constructed by piece-wise continuous 1D inversions. Shear-velocity contours are separated by 200 m/s.

Declaration of Competing Interests

The authors acknowledge there are no conflicts of interest recorded.

Acknowledgments

The authors thank Dylan Mikesell and an anonymous reviewer for improving the context of the article. The authors thank Elizabeth Berg, Sin-Mei Wu, Jamie Farrell, and Jim Pechmann for constructive discussions through this study. The authors thank Kevin Mendoza, Monique Holt, Elizabeth Berg, Clay Woods, and the students of the University of Utah class "Seismic Imaging II" (Spring 2018) for their help during the deployment of the nodal stations and homeowners who volunteered to host nodal stations. This study was supported by the National Science Foundation Grant EAR 1753362. K. G. acknowledges a scholarship by the Alexander S. Onassis Foundation (Scholarship ID: F ZO 02-1/2018–2019).

References

Allam, A. A., and Y. Ben-Zion (2012). Seismic velocity structures in the southern California plate-boundary environment from double-difference tomography, *Geophys. J. Int.* **190,** no. 2, 1181–1196.

Ampuero, J. P., and X. Mao (2017). Upper limit on damage zone thickness controlled by seismogenic depth, in *Fault Zone Dynamic Processes: Evolution of Fault Properties during Seismic Rupture*, Vol. 227, 243.

Bashore, W. M. (1982). Upper crustal structure of the Salt Lake Valley and the Wasatch fault from seismic modeling, *M. S. Thesis*, University of Utah, Salt Lake City, Utah, 95 pp.

Behera, L., P. Khare, and D. Sarkar (2011). Anisotropic *P*-wave velocity analysis and seismic imaging in onshore Kutch sedimentary basin of India, *J. Appl. Geophys.* **74,** no. 4, 215–228.

Ben-Zion, Y., and C. G. Sammis (2003). Characterization of fault zones, *Pure Appl. Geophys.* **160,** nos. 3/4, 677–715.

Berg, E. M., F. C. Lin, A. Allam, V. Schulte-Pelkum, K. M. Ward, and W. Shen (2020). Shear velocity model of Alaska via joint inversion of Rayleigh wave ellipticity, phase velocities, and receiver functions across the Alaska transportable array, *J. Geophys. Res.* **125,** no. 2, e2019JB018582, doi: 10.1029/2019JB018582.

Berg, S. S., and T. Skar (2005). Controls on damage zone asymmetry of a normal fault zone: Outcrop analyses of a segment of the Moab fault, SE Utah, *J. Struct. Geol.* **27,** no. 10, 1803–1822, doi: 10.1016/j.jsg.2005.04.012.

Bose, S., and S. Mitra (2010). Analog modeling of divergent and convergent transfer zones in listric normal fault systems, *AAPG Bulletin* **94,** no. 9, 1425–1452, doi: 10.1306/01051009164.

Bowden, D. C., V. C. Tsai, and F. C. Lin (2015). Site amplification, attenuation, and scattering from noise correlation amplitudes across a dense array in Long Beach, CA, *Geophys. Res. Lett.* **42,** no. 5, 1360–1367, doi: 10.1002/2014GL062662.

Brenguier, F., P. Kowalski, N. Ackerley, N. Nakata, P. Boué, M. Campillo, E. Larose, S. Rambaud, C. Pequegnat, T. Lecocq, *et al.* (2016). Toward 4D noise-based seismic probing of volcanoes: Perspectives from a large-*N* experiment on Piton de la Fournaise Volcano, *Seismol. Res. Lett.* **87,** no. 1, 15–25.

Brocher, T. M. (2005). Empirical relations between elastic wavespeeds and density in the Earth's crust, *Bull. Seismol. Soc. Am.* **95,** no. 6, 2081–2092, doi: 10.1785/0120050077.

Buddensiek, M. L., J. Sheng, T. Crosby, G. T. Schuster, R. L. Bruhn, and R. He (2008). Colluvial wedge imaging using traveltime and waveform tomography along the Wasatch fault near Mapleton, Utah, *Geophys. J. Int.* **172,** no. 2, 686–697.

Castellanos, J. C., R. W. Clayton, and A. Juarez (2020). Using a time-based subarray method to extract and invert noise-derived body waves at Long Beach, California, *J. Geophys. Res.* **125,** no. 5, e2019JB018855.

Clayton, R. W. (2020). Imaging the subsurface with ambient noise autocorrelations, *Seismol. Res. Lett.* **91,** 930–935, doi: 10.1785/0220190272.

Davison, I. (1986). Listric normal fault profiles: Calculation using bed-length balance and fault displacement, *J. Struct. Geol.* **8,** no. 2, 209–210.

De Ridder, S. A. L., and B. L. Biondi (2013). Daily reservoir-scale subsurface monitoring using ambient seismic noise, *Geophys. Res. Lett.* **40,** no. 12, 2969–2974.

DuRoss, C. B., S. F. Personius, A. J. Crone, S. S. Olig, M. D. Hylland, W. R. Lund, and D. P. Schwartz (2016). Fault segmentation: New concepts from the Wasatch fault zone, Utah, USA, *J. Geophys. Res.* **121,** no. 2, 1131–1157.

Faulkner, D. R., T. M. Mitchell, E. Jensen, and J. Cembrano (2011). Scaling of fault damage zones with displacement and the implications for fault growth processes, *J. Geophys. Res.* **116,** no. B5, doi: 10.1029/2010JB007788.

Finzi, Y., E. H. Hearn, Y. Ben-Zion, and V. Lyakhovsky (2009). Structural properties and deformation patterns of evolving strike-slip faults: Numerical simulations incorporating damage rheology, *Pure Appl. Geophys.* **166,** nos. 10/11, 1537–1573.

Flodin, E., and A. Aydin (2004). Faults with asymmetric damage zones in sandstone, Valley of Fire State Park, southern Nevada, *J. Struct. Geol.* **26,** no. 5, 983–988.

Fu, H., C. He, B. Chen, Z. Yin, Z. Zhang, W. Zhang, T. Zhang, W. Xue, W. Liu, W. Yin, *et al.* (2017). 9-Pflops nonlinear earthquake simulation on Sunway Taihu Light: Enabling depiction of 18-Hz and 8-meter scenarios, *Proc. of the International Conf. for High Performance Computing, Networking, Storage and Analysis*, 1–12.

Gilbert, G. K. (1890). *Lake Bonneville*, United States Geological Survey, Monographs, Vol. 1, U.S. Government Printing Office, Washington, DC, 438 pp.

Graves, R. W., B. T. Aagaard, and K. W. Hudnut (2011). The ShakeOut earthquake source and ground motion simulations, *Earthq. Spectra* **27,** no. 2, 273–291.

Herrmann, R. B. (2013). Computer programs in seismology: An evolving tool for instruction and research, *Seismol. Res. Lett.* **84,** no. 6, 1081–1088.

Hill, J., H. Benz, M. Murphy, and G. Schuster (1990). Propagation and resonance of *SH*waves in the Salt Lake Valley, Utah, *Bull. Seismol. Soc. Am.* **80,** no. 1, 23–42.

Hu, X., Z. Lu, and T. Wang (2018). Characterization of hydrogeological properties in Salt Lake Valley, Utah, using InSAR, *J. Geophys. Res.* **123,** no. 6, 1257–1271.

Johnson, L. R., and W. Silva (1981). The effects of unconsolidated sediments upon the ground motion during local earthquakes, *Bull. Seismol. Soc. Am.* **71,** no. 1, 127–142.

Keifer, I., K. Dueker, and P. Chen (2019). Ambient Rayleigh wave field imaging of the critical zone in a weathered granite terrane, *Earth Planet. Sci. Lett.* **510,** 198–208.

Kowalewska, A., and A. S. Cohen (1998). Reconstruction of paleoenvironments of the Great Salt Lake basin during the late Cenozoic, *J. Paleolimnol.* **20,** no. 4, 381–407.

Leung, A. Y. T., and R. K. L. Su (1996). Analytical solution for mode I crack orthogonal to free surface, *Int. J. Fract.* **76,** no. 1, 79–95.

Li, G., H. Chen, F. Niu, Z. Guo, Y. Yang, and J. Xie (2016). Measurement of Rayleigh wave ellipticity and its application to the joint inversion of high-resolution *S* wave velocity structure beneath northeast China, *J. Geophys. Res.* **121,** no. 2, 864–880.

Li, J., F. C. Lin, A. Allam, Y. Ben-Zion, Z. Liu, and G. Schuster (2019). Wave equation dispersion inversion of surface waves recorded on irregular topography, *Geophys. J. Int.* **217,** no. 1, 346–360.

Liberty, L. M., J. S. Clair, and G. Gribler (2018a). Seismic landstreamer data reveal complex tectonic structures beneath Salt Lake City, *SEG Technical Program Expanded Abstracts 2018*, Society of Exploration Geophysicists, 2662–2666.

Liberty, L. M., J. S. Clair, and G. Gribler (2018b). *Seismic profiling in downtown Salt Lake City: Mapping the Wasatch fault with seismic velocity and reflection methods from a land streamer, U.S. Geol. Surv. Award G17AP00052 Rept.*, 47 pp., available at https://earthquake.usgs.gov/cfusion/external_grants/reports/G17AP00052.pdf (last accessed February 2021).

Lin, F.-C. (2018). *Salt Lake Linear Nodal Array 2018 [Data set]*, International Federation of Digital Seismograph Networks, doi: 10.7914/SN/9H_2018.

Lin, F. C., D. Li, R. W. Clayton, and D. Hollis (2013). High-resolution 3D shallow crustal structure in Long Beach, California: Application of ambient noise tomography on a dense seismic array, *Geophysics* **78,** no. 4, Q45–Q56.

Lin, F.-C., M. H. Ritzwoller, and R. Snieder (2009). Eikonal tomography: Surface wave tomography by phase-front tracking across a regional broad-band seismic array, *Geophys. J. Int.*, doi: 10.1111/j.1365-246X.2009.04105.x.

Lobkis, O. I., and R. L. Weaver (2001). On the emergence of the Green's functionin the correlations of a diffuse field, *J. Acoust. Soc. Am.* **110,** 3011–3017.

Lyakhovsky, V., and Y. Hamiel (2007). Damage evolution and fluid flow in poroelastic rock, *Izvestiya Phys. Solid Earth* **43,** no. 1, 13–23.

Ma, Y., R. W. Clayton, V. C. Tsai, and Z. Zhan (2013). Locating a scatterer in the active volcanic area of southern Peru from ambient noise cross-correlation, *Geophys. J. Int.* **192,** no. 3, 1332–1341.

Mabey, D. R. (1992). Subsurface geology along the Wasatch front, in *Assessment of Earthquake Hazards and Risk Along the Wasatch Front, Utah*, P. L. Goriand and W. W. Hays (Editors), U.S. Geol. Surv. Pro. Pap. 1500-A-J, C1–C16.

Magistrale, H., J. Pechmann, and K. Olsen (2009). The Wasatch front, Utah, community seismic velocity model, *Seismol. Res. Lett.* **80,** 368.

McDonald, G. N., and F. X. Ashland (2008). *Earthquake Site Conditions in the Wasatch Front Corridor, Utah*, Utah Geological Special Study, Vol. 125, 41 pp., 1 plate, scale 1:150,000.

McDonald, G. N., E. J. Kleber, A. I. Hiscock, S. E. K. Bennett, and S. D. Bowman (2020). Fault trace mapping and surface-fault-rupture special study zone delineation of the Wasatch fault zone, Utah and Idaho, *Utah Geol. Surv. Investig. Rept. 280*, 23 pp., doi: 10.34191/RI-280.

McKean, A. P. (2018). Interim geologic map of the Sugar House quadrangle, Salt Lake County, Utah, *Utah Geol. Surv. Open-File Rept. 687DM*, 2 plates, scale 1:24,000, 28 pp.

Mohapatra, G. K., and R. A. Johnson (1998). Localization of listric faults at thrust fault ramps beneath the Great Salt Lake Basin, Utah: Evidence from seismic imaging and finite element modeling, *J. Geophys. Res.* **103,** no. B5, 10,047–10,063.

Molli, G., G. Cortecci, L. Vaselli, G. Ottria, A. Cortopassi, E. Dinelli, M. Mussi, and M. Barbieri (2010). Fault zone structure and fluid–rock interaction of a high angle normal fault in Carrara marble (NW Tuscany, Italy), *J. Struct. Geol.* **32,** no. 9, 1334–1348.

Mordret, A., P. Roux, P. Boué, and Y. Ben-Zion (2019). Shallow three-dimensional structure of the San Jacinto fault zone revealed from ambient noise imaging with a dense seismic array, *Geophys. J. Int.* **216,** no. 2, 896–905.

Morey, D., and G. T. Schuster (1999). Paleoseismicity of the Oquirrh fault, Utah from shallow seismic tomography, *Geophys. J. Int.* **138,** 25–35.

Moschetti, M. P., S. Hartzell, L. Ramírez-Guzmán, A. D. Frankel, S. J. Angster, and W. J. Stephenson (2017). 3D ground-motion simulations of M_w 7 earthquakes on the Salt Lake City segment of the Wasatch fault zone: Variability of long-period ($T \geq 1$ s) ground motions and sensitivity to kinematic rupture parameters, *Bull. Seismol. Soc. Am.* **107,** no. 4, 1704–1723.

Nakata, N., P. Boué, F. Brenguier, P. Roux, V. Ferrazzini, and M. Campillo (2016). Body and surface wave reconstruction from seismic noise correlations between arrays at Piton de la Fournaise volcano, *Geophys. Res. Lett.* **43,** no. 3, 1047–1054.

Nakata, N., J. P. Chang, J. F. Lawrence, and P. Boué (2015). Body wave extraction and tomography at Long Beach, California, with ambient-noise interferometry, *J. Geophys. Res.* **120,** no. 2, 1159–1173.

Olig, S. S., W. R. Lund, B. D. Black, and B. H. Mayes (1996). Paleoseismic investigation of the Oquirrh fault zone, Tooele County, Utah, *Utah Geol. Surv. Spec. Study* **88,** 22–54.

Oviatt, C. G. (2015). Chronology of Lake Bonneville, 30,000 to 10,000 yr BP, *Quaternary Sci. Rev.* **110,** 166–171.

Pang, G., K. D. Koper, M. Mesimeri, K. L. Pankow, B. Baker, J. Farrell, J. Holt, J. M. Hale, P. Roberson, R. Burlacu, *et al.* (2020). Seismic analysis of the 2020 Magna, Utah, earthquake sequence: Evidence for a listric Wasatch fault, *Geophys. Res. Lett.* **47,** no. 18, e2020GL089798.

Perrin, C., I. Manighetti, J. P. Ampuero, F. Cappa, and Y. Gaudemer (2016). Location of largest earthquake slip and fast rupture controlled by along-strike change in fault structural maturity due to fault growth, *J. Geophys. Res.* **12,** no. 5, 3666–3685.

Petersen, M. D., A. M. Shumway, P. M. Powers, C. S. Mueller, M. P. Moschetti, A. D. Frankel, S. Rezaeian, D. E. McNamara, N. Luco, O. S. Boyd, *et al.* (2020). The 2018 update of the US National Seismic Hazard Model: Overview of model and implications, *Earthq. Spectra* **36,** no. 1, 5–41.

Prudencio, M., and M. V. S. Jan (2007). Strength and failure modes of rock mass models with non-persistent joints, *Int. J. Rock Mech. Min. Sci.* **44,** no. 6, 890–902.

Radkins, H., M. Murphy, and G. Schuster (1989). Subsurface map and seismic risk analysis of the Salt Lake Valley, *Utah Geological and*

Mineral Survey Report, Contract 5-24496, available at https://ugspub.nr.utah.gov/publications/open_file_reports/OFR-152.pdf (last accessed February 2021).
Ranasinghe, N. R., L. L. Worthington, C. Jiang, B. Schmandt, T. S. Finlay, S. L. Bilek, and R. C. Aster (2018). Upper-crustal shear-wave velocity structure of the south-central Rio Grande rift above the Socorro magma body imaged with ambient noise by the large-*N* Sevilleta seismic array, *Seismol. Res. Lett.* **89,** no. 5, 1708–1719.
Roux, P., L. Moreau, A. Lecointre, G. Hillers, M. Campillo, Y. Ben-Zion, D. Zigone, and F. Vernon (2016). A methodological approach towards high-resolution surface wave imaging of the San Jacinto fault zone using ambient-noise recordings at a spatially dense array, *Geophys. J. Int.* **206,** no. 2, 980–992.
Sagy, A., E. E. Brodsky, and G. J. Axen (2007). Evolution of fault-surface roughness with slip, *Geology* **35,** no. 3, 283–286.
Shapiro, N. M., M. Campillo, L. Stehly, and M. H. Ritzwoller (2005). High-resolution surface-wave tomography from ambient seismic noise, *Science* **307,** no. 5715, 1615–1618.
Shen, W., M. H. Ritzwoller, and V. Schulte-Pelkum (2013). A 3-D model of the crust and uppermost mantle beneath the central and western US by joint inversion of receiver functions and surface wave dispersion, *J. Geophys. Res.* **118,** no. 1, 262–276.
Shimeld, J., Q. Li, D. Chian, N. Lebedeva-Ivanova, R. Jackson, D. Mosher, and D. Hutchinson (2016). Seismic velocities within the sedimentary succession of the Canada basin and southern Alpha–Mendeleev ridge, Arctic Ocean: Evidence for accelerated porosity reduction? *Geophys. J. Int.* **204,** no. 1, 1–20.
Spica, Z., M. Perton, M. Calò, D. Legrand, F. Córdoba-Montiel, and A. Iglesias (2016). 3-D shear wave velocity model of Mexico and south US: Bridging seismic networks with ambient noise cross-correlations (C^1) and correlation of coda of correlations (C^3), *Geophys. J. Int.* **206,** no. 3, 1795–1813.
Stokes, W. L. (1980). Geologic setting of Great Salt Lake, *Great Salt Lake* **116,** 54.
Thakur, P., Y. Huang, and Y. Kaneko (2020). Effect of fault damage zones on long-term earthquake behavior on mature strike-slip faults, *J. Geophys. Res.* doi: 10.1029/2020JB019587.
Thomas, A. M., Z. Spica, M. Bodmer, W. H. Schulz, and J. J. Roering (2020). Using a dense seismic array to determine structure and site effects of the two towers earthflow in northern California, *Seismol. Res. Lett.* **91,** no. 2A, 913–920.
Tinsley, J. C., K. W. King, D. A. Trumm, D. L. Carver, and R. Williams (1991). Geologic aspects of shear-wave velocity and relative ground response in Salt Lake Valley, Utah, *Proc. of the 27th Symposium on Engineering Geology and Geotechnical Engineering*, 25-1–25-9.
Twiss, R. J., R. J. Twiss, and E. M. Moores (1992). *Structural Geology*, R. J. Twiss and E. M. Moores (Editors), W. H. Freeman & Co., San Francisco, 532 pp., doi: 10.1002/gj.3350290408.
Wang, Y., A. Allam, and F.-C. Lin (2019b). Imaging the fault damage zone of the San Jacinto fault near Anza with Ambient noise tomography using a Dense Nodal array, *Geophys. Res. Lett.* **46,** doi: 10.1029/2019GL084835.
Wang, Y., F. C. Lin, B. Schmandt, and J. Farrell (2017). Ambient noise tomography across Mount St. Helens using a dense seismic array, *J. Geophys. Res.* **122,** no. 6, 4492–4508.
Wang, Y., F. C. Lin, and K. M. Ward (2019a). Ambient noise tomography across the Cascadia subduction zone using dense linear seismic arrays and double beamforming, *Geophys. J. Int.* **217,** no. 3, 1668–1680.
Wang, Z. (2001). Fundamentals of seismic rock physics, *Geophysics* **66,** no. 2, 398–412.
Wernicke, B. (1981). Low-angle normal faults in the Basin and Range Province: Nappe tectonics in an extending orogeny, *Nature* **291,** no. 5817, 645–648.
Wu, S. M., F. C. Lin, J. Farrell, and A. Allam (2019). Imaging the deep subsurface plumbing of Old Faithful geyser from low-frequency hydrothermal tremor migration, *Geophys. Res. Lett.* **46,** no. 13, 7315–7322.
Wu, S. M., F. C. Lin, J. Farrell, B. Shiro, L. Karlstrom, P. Okubo, and K. Koper (2020). Spatiotemporal seismic structure variations associated with the 2018 Kīlauea eruption based on temporary dense geophone arrays, *Geophys. Res. Lett.* **47,** no. 9, e2019GL086668.
Wu, S. M., K. M. Ward, J. Farrell, F. C. Lin, M. Karplus, and R. B. Smith (2017). Anatomy of old faithful from subsurface seismic imaging of the Yellowstone Upper Geyser Basin, *Geophys. Res. Lett.* **44,** no. 20, 10–240.
Xu, S., E. Fukuyama, Y. Ben-Zion, and J. P. Ampuero (2015). Dynamic rupture activation of backthrust fault branching, *Tectonophysics* **644,** 161–183.

Manuscript received 29 October 2020
Published online 10 March 2021